Spatially Regulated Gas Flow Control for Batch-Drying of Large Area Slot-Die-Coated Perovskite Thin Films

Kristina Geistert, Ronja Pappenberger, Philip Scharfer, Philipp Cavadini, Wilhelm Schabel, Faranak Sadegh, David B. Ritzer, Bahram Abdollahi Nejand, and Ulrich W. Paetzold*

Innovations in scalable fabrication processes are pivotal for transferring record power conversion efficiencies (PCEs) of spin-coated perovskite/silicon-based tandem solar cells (TSCs) from the laboratory scale to full-size photovoltaics. In this regard, the homogeneous large-area drying of precursor ink wet films poses one of the major hurdles. Gas-assisted drying by linear high-pressure slot jets comes along with an inhomogeneous flow field, causing unwanted backflows, non-uniform drying patterns, and strong inhomogeneities at the sample edges. In response, it is demonstrated i) a new 2D comb-nozzle (CN) drying technique that improves the homogeneity of drying processes and, ii) an adjusted strategy to fabricate high-quality 2-step slot-die (SD)-coated triple-halide perovskite thin films. Remarkably, homogeneous and pinhole-free large-area SD-coated perovskite SCs fabricated is demonstrated with all scalable techniques reaching up to 19.6% with enhanced mean PCE-yields of 90% (compared to 62% with slot-jet drying). Consequently, the CN drying method is employed for a material composition suitable for tandem applications ($E_g \approx 1.68$ eV). Particularly, the reproducible fabrication of TSCs with PCEs up to 24.6% on large areas with homogeneous PCE variances of $\pm 0.7\%_{abs}$ imply high homogeneity during the coating and drying process and confirms the importance of systematically controlled drying within an optimized 2-step process.

1. Introduction

Next-generation photovoltaics (PVs) encompassing new semiconductor materials experience a great interest in research and industry.[1–5] Perovskite solar cells (PSCs) are one of the most promising emerging thin-film technologies and have shown impressive technological development in the last 15 years. In 2023, PSCs reached power conversion efficiencies (PCEs) comparable to established crystalline Si solar panels due to the outstanding optoelectronic characteristics of the hybrid organic-inorganic perovskite semiconductor materials.[6,7] These characteristics include short absorption lengths, long charge carrier diffusion lengths, defect tolerance as well as their bandgap tunability, and the ease and potential of fabrication by solution-based deposition techniques.[8–10] In addition, PSCs synergizing with silicon PV in tandem configurations using low-cost production hold great potential for the solar energy industry.[7] However, to date, scaling up the device production without losing in performance remains a major hurdle.

Therefore, upscaling the deposition of homogeneous high-quality thin films to large areas (≥ 100 cm^2) without performance loss using industry-relevant deposition techniques, is a research topic of utmost importance.[2,11–14] The present work addresses the drying of solution-processed scalable hybrid perovskite thin film depositions, namely inkjet printing, blade coating, and slot-die coating (SDC), exemplary with the SDC technique. SDC is a pre-metered coating technique, during which the precursor solution transferred to the substrate is controlled by a supply system, achieving a precise, uniform deposition of a wet thin film within a certain thickness. It has a high flexibility regarding the range of processable solution viscosities, a high material efficiency, and is compatible with industrially relevant roll-to-roll (R2R) production.[15,16] Therefore, SDC is considered one of the most versatile techniques used for coating by solution processing.[14,16,17] Altogether, SDC promises scalable, material- and cost-efficient deposition of perovskite thin films on a wide range of substrate types.[10,18,17]

Upscaling losses in solution-processed perovskite PV modules still remain high compared to concurrent thin-film modules

K. Geistert, R. Pappenberger, F. Sadegh, D. B. Ritzer, U. W. Paetzold
Light Technology Institute
Karlsruhe Institute of Technology (KIT)
76131 Karlsruhe, Germany
E-mail: ulrich.paetzold@kit.edu
K. Geistert, R. Pappenberger, F. Sadegh, D. B. Ritzer, U. W. Paetzold
Institute of Microstructure Technology
KIT
76344 Eggenstein-Leopoldshafen, Germany
P. Scharfer, P. Cavadini, W. Schabel
Thin Film Technology (TFT)
KIT
76344 Eggenstein-Leopoldshafen, Germany
B. Abdollahi Nejand
Meyer Burger (Germany) AG
An d. Baumschule 6-8, 09337 Hohenstein-Ernstthal, Germany

**ADVANCED
SCIENCE NEWS**

www.advancedsciencenews.com

**ADVANCED
ENERGY
MATERIALS**

www.advenergymat.de

involving similar architectures, even considering inevitable scribing losses during large-scale fabrication.[9,13] Losses due to inhomogeneity occur, especially on sample edges, due to entangled stages of drying, nucleation, and grain growth.[19] The reason is that the morphology formation and thickness evolution are more complex to control during the perovskite thin film formation compared to centrifugal force-regularized spin-coating processes. Due to the higher solvent content and increased drying time in these wet thin films, complex fluidics, drying, and crystallization dynamics of perovskite solution thin films are more present in scalable depositions.[20] Consequently, the impact of drying-related transport mechanisms and phenomena, such as the coffee ring effect is magnified in these thicker thin films, challenging the sufficient control of the drying process. The diminished control during drying often results in inhomogeneous fluid dynamics, concretely causing unwanted backflows and severe edge effects. Moreover, inconsistently distributed drying rates create ununiform drying patterns with different lateral properties.[21] Altogether, this causes low operational stability when fabricating larger areas.[21,10] Therefore, the most challenging part of upscaling PSCs is not the deposition itself, but the precise drying of a perovskite thin film, resulting in a homogeneous thin-film morphology over a large area and is, to date, a subject of current research, e.g. to advance to tandem technology.[22]

As a consequence, the major challenge of solution-processed large-area thin-film fabrication is selecting the most suitable quenching and drying technique. The desired properties of such a thin film include full surface coverage without pinholes, low roughness, high crystallinity, and low density of grain boundaries.[23,20] Three methods are widely applied – vacuum, antisolvent, and gas-assisted quenching.[24,14] Gas-assisted quenching and drying is a facile, reproducible, low-cost, and easily transferable technique, therefore holding great potential for applications of highly efficient large-area PSCs as recently demonstrated on slot-die coated wide-bandgap perovskite PV by Matondo et al.[12,24,25,26] Thereby, the essential role of the gas quenching treatment is achieving a smooth and compact perovskite film by controlling the nucleation rate which could be lately validated via in situ optical spectroscopies integrated into a doctor-blading setup facilitating real-time monitoring of thin film formation during the gas-quenching process.[27] A current review from Azhar et al. emphasizes its potential to become the preferred method for industrial PSC production in highlighting the performance benefits, environmental impact, and commercial scalability of gas quenching.[28] Recent advances in gas quenching are shown during spin coating as the innovative utilization of methylamine, propylamine hydrochloride, or additional ultrasonic-assisted processing combined with gas quenching to enhance the grain size of the perovskite film, reduce grain boundary defects, and suppress carrier nonradiative recombination, improving carrier extraction and transport.[29,30,31] Finally, very recent advancements of gas-assisted drying on slot-die coated devices are shown by Duarte et al. via additional heating of the substrate, creating a temperature gradient that suppresses vertical crystal growth, promoting smoother, horizontal growth, and, therefore, resulting in better surface coverage.[10] Our prior studies focus on the understanding of gas-assisted, controlled removal of solvents as a promising scalable fabrication method

to fabricate high-efficiency cells without the costly and complex handling of antisolvents and vacuum-induced quenching.[10,32–34] In a nutshell, we showed that controlled and promptly induced nucleation-rich drying is crucial to achieve high PCEs for large-area solution-processed multi-cation perovskite thin films by in situ monitoring of the morphology formation of 1-step processed perovskite thin films underneath a single narrow slot jet.[24,34] We further validated that there is a specifically high solvent mass transfer needed at the lateral positions where the wet thin film passes the critical solute concentration to remove the solvent promptly, inducing rapid drying and high nucleation rates.[11,25,33–36] Such a high mass transfer is provided only directly underneath the slot jet.[37,38] To date, we have achieved one of the lowest absolute upscaling losses for SD-coating ($-0.66\%_{abs}$/dec.) with this methodology. However, the high-pressure, 1D technique still comes with inhomogeneous gas dynamics causing fluidic backflows, ununiform drying patterns, and especially unintentional severe drying effects on the edges, because of complex disturbances of the gas flow.[39,40]

Regarding these drawbacks, part of our solution is reducing the sufficient mass transfer, leveraging on the knowledge that mass transfers for quenching of 1-step depositions are significantly higher than for 2-step methods. 2-step routes provide regular perovskite thin film crystallization on a laboratory scale in several prior works.[18,41,42] The methodology of first, depositing inorganics and second, organics as separate precursor solutions, needs a significantly lower mass transfer during gas-assisted drying and therefore allows to "only" homogeneously remove a high amount of low-boiling point solvents after the second deposition step. In addition, greater flexibility in perovskite composition and solvents complements facilitating high-quality large-area solution depositions such as SDC.[10,14,41,43] In 2020, two-step sequential blade-coating was employed for the scalable fabrication of FA-based perovskite solar cells from ≈0.1 cm² devices (20.49%) to 100 cm² modules (13.32%) in a work of Zhang et al. The research group facilitates the self-formation of regular nano-porous structured PbI₂ thin films during blade-coating with a non-volatile solvent having strong coordination and low solubility with PbI₂. Further, they developed a proper perovskite seed-assisted growth to improve the crystallinity, altogether effectively converting the precursor material system to black phase perovskites.[44] Recent advancements in two-step coating methods for perovskite fabrication can be leveraged in the works of Chang et al., introducing the additive methylammonium chloride (MACl) in the second step to modulate the crystallization and orientation of a two-step sequential doctor-bladed perovskite thin film in ambient conditions.[45] Another research by Chang et al. provides a strategy for constructing a high-performance interface bridge between tin oxide SnO₂ and the perovskite thin film. They encounter the problem that defects are distributed at the buried interface by incorporating 2-(N-morpholino)ethanesulfonic acid potassium salt (MESK) as the bridging layer between the SnO₂ electron transport layer (ETL) and the perovskite thin film deposited via scalable two-step deposition, demonstrating that MESK can passivate trap states of Sn suspension bonds.[46]

Given the extensive innovative research studies, this work also focuses on 2-step processes as a promising route to fabricate uniform and high-quality perovskite thin films as well as on the crucial precise drying on the large area without needing high mass

ADVANCED
SCIENCE NEWS

www.advancedsciencenews.com

ADVANCED
ENERGY
MATERIALS

www.advenergymat.de

transfers for scalable industrial fabrication lines as elaborated priorly.

In response, we adjust a previously proposed drying system for 2-step processed perovskite thin films. The system adapts a concept developed before in other contexts by Cavadini et al.[47,48] The CN dryer controls the challenging gas flow over a $20 \times 20\,cm^2$ nozzle array of impinging hexagon-shaped jets purged with inert gas (gas outlets) surrounded by suction holes (gas inlets), such that precisely defined drying rates are established. We compare the results of dried perovskite thin films with more conventional slot jet drying which provides one high-pressure nozzle and investigate the dependence of the perovskite drying and crystallization on the local gas flow. The present work focuses on the control and influence of drying rates over the 2D area, pushing large-area homogeneous drying processes for different material systems of SD-coated 2-step deposited triple-cation (MA, FA, and Cs) perovskite thin films. The consistent evaluation of the morphology formation and PCE yield leads to crucial and concrete rectification work on the drying procedure, finally resulting in the successful fabrication of scalable SD-coated gas-assisted dried (tandem) SCs and modules with only minimal upscaling losses. Particularly, perovskite/silicon tandem devices with PCEs up to 24.6% and homogeneous PCE distribution ($\pm\,0.7\%_{abs}$) without discarding any part of the original substrate, confirm the importance of a systematically controlled drying technique within the optimized 2-step process. Validating the advantages of a systematic, 2D, and flow-optimized gas-assisted drying system, this is a cornerstone preventing expensive brute force optimization.

2. Results and Discussion

2.1. The Way to Comb Nozzle Drying

To investigate the perovskite morphology processed with a novel drying system on large areas (i.e., $\geq 100\,cm^2$), we present a unique setup to define precise process parameters (e.g., gas speed, mass/heat transfer, and drying height) and compare the associated perovskite thin film quality with commonly used slot jet drying (**Figure 1**). The main advance lies in the precise drying conditions being defined via a movable dryer hood with a $20 \times 20\,cm^2$ nozzle array pattern consisting of hexagon-shaped jets (gas outlets) surrounded by suction slits (gas inlets). Thereby, the equally distributed gas inlets ensure local removal of the drying air to adjust heat/mass transfer coefficients.

The perovskite absorber layer is processed in a 2-step process from solution via SDC (Figure 1a,b). The 2-step route generally includes the subsequent deposition of first, the Pb-containing precursor materials and second, the organic cations feasible in low boiling point solvents. Details about the specific 2-step processed precursor material composition and SDC parameters can be found in the experimental section. The Pb-containing precursor solutions (inorganic layer) are additionally altered by a 5 vol% L-α-Phosphatidylcholine (α-LP) solution, increasing the adhesion of the inorganic inks to the underlying charge transport layer.[49] Furthermore, the surfactant α-LP suppresses the solution flow (and therefore, directional movement of particles) toward islands of dried material, altering the fluid drying dynamics, and leading to a uniform, yellow-transparent layer (see experimental section). After the second deposition step, the resulting

wet film is – as a reference – dried with a single narrow slot jet of 10 cm width, height H_D, angle β, slot width $b_D = 50\,\mu m$, gas flow rate u_0, and drying velocity v_2 (Figure 1c,e and a more detailed schematic are shown in the Supporting Information, Figure S1). In regard to the fluidic distribution, given a suitable wettability, the most consistent homogenous drying results are provided when the gas backflow can be reduced (Figure 1e, marked in red). As a result, we improved gas backflow prevention by setup adjustments in a prior work, in order to enlarge the optimal area for a 1-step route.[34] According adjustments result in the minimized gas backflow for the presented setup and mainly include an increased overlapping of the slot jet lips (0.5 cm), exact control of the angle β (15°), and optimal distance of the drying slot jet H_D (0.3 cm) toward the substrate (optimized on a slot width of 50 μm, indicated in Figure 1e).[34] The optimized drying process parameters and mechanical adjustments for unobstructed gas flows can be employed to the 2-step route of the current work and are only slightly adjusted by changing the gas flow rate u_0 and drying velocity v_2 for the respective material system. Nevertheless, a certain proportion of the gas backflow is inevitable, due to disturbing, but important functions and thereby difficult to eliminate components in the nozzle. Additionally, the inside contour having edges and certain radii of curvature inducing stalling and turbulences of the gas flow as well as the tendency of air flowing from high to low pressure regions induce turbulent gas backflows.[39,40] These factors can lead to severe edge effects, and fluidic backflows by pushed-back wet films and dried thin films with different lateral properties and are, to date, a major challenge.

As a response to control the drying and crystallization dynamics of the SD-coated perovskite wet thin film, we propose a comb nozzle (CN) drying technique for SD-coated 2-step processed triple-halide perovskite absorbers with gas in- and outlets (Figure 1d). Regarding industrial drying methods, arrays of round or slot nozzles suffer from large deviations of the local heat and mass transfer coefficients in lateral directions. Due to the complexity of the formation of polycrystalline perovskite thin films from the precursor solution, mentioned in the introduction above, efficient strategies for process transfer require advancing the precise control of drying rates. We demonstrate the deployment of homogenous drying with sufficient drying parameters, which obtain the intended crystallization but still do not disturb the high-quality homogeneity. Specifically, drying conditions are defined via a $20 \times 20\,cm^2$ nozzle array pattern consisting of hexagon-shaped jets (gas outlets) surrounded by suction slits (gas inlets) for the local removal of the drying air to adjust heat/mass transfer coefficients (Figure 1f and a photograph of the comb nozzle (CN) dryer hood is shown in, Figure S2, Supporting Information). Latter heat/mass transfer coefficients are figures of merit for the solvent removal on the sample surface and are priorly validated.[47,48,50,51] Drying rates are precisely controlled with a height H_{CN} in the range of 8 to 24 mm, a drying gas temperature T_{CN} in the range of 40–100 °C and ejection of the GB inert atmosphere with heat transfer coefficient α_{CN} up to 124 W m^{-2} K^{-1} (at 8 mm) which range is dependent on H_{CN}. During this work, the drying temperature of the movable table T_D is always adjusted to the corresponding drying gas temperature T_{CN}.[47,48] First, numerical optimization was performed on the pattern of the array of impinging jets and its supply system. Second, the resulting design was validated and characterized through experimental
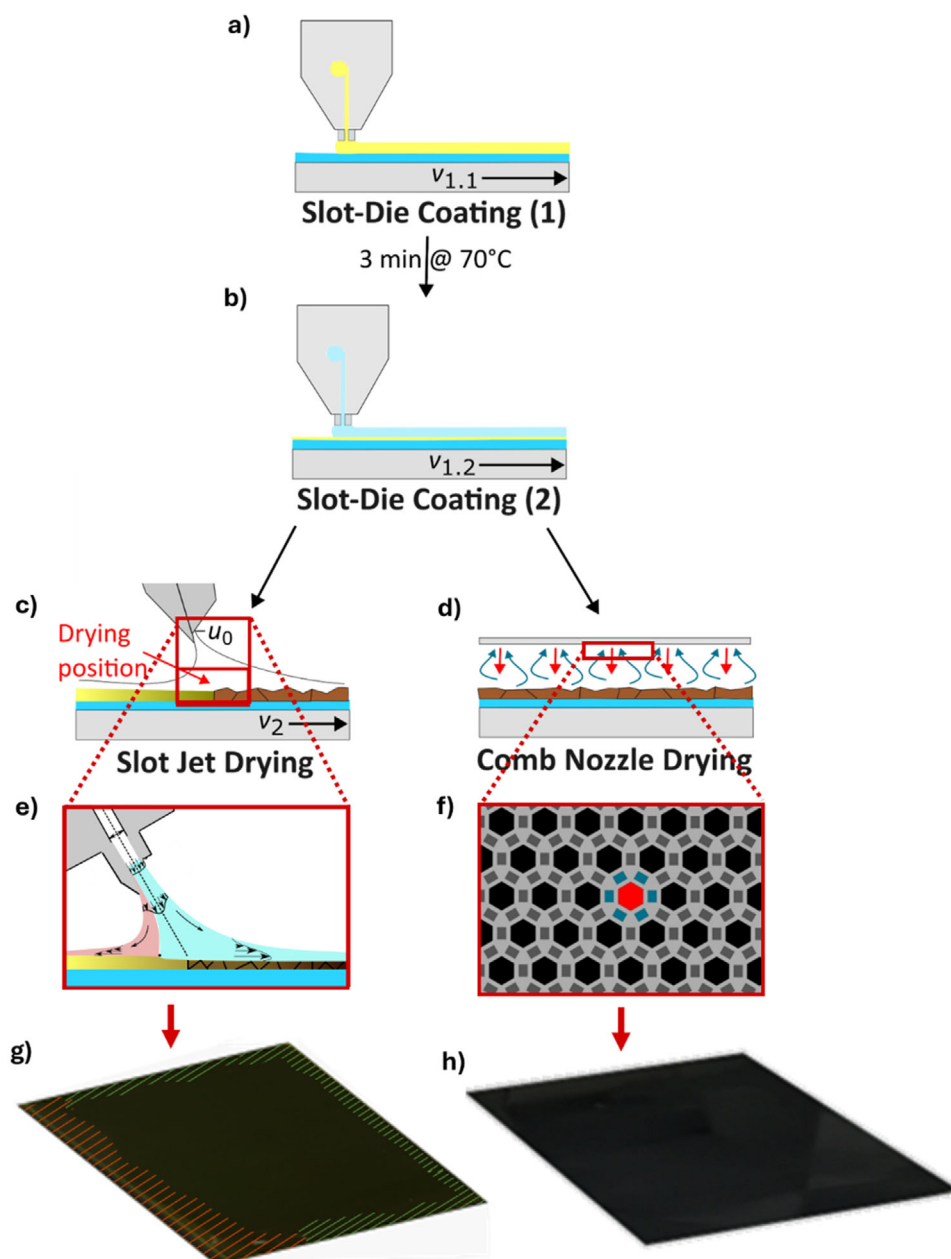
Figure 1. Schematic of first, slot-die coating (SDC) inorganics a), a heating step (3 min @ 70°C) and second SDC organics b) using two respective velocities $v_{1.1}$ and $v_{1.2}$ with subsequent dynamic gas-assisted slot jet drying c) with drying velocity v_2. Drying is performed with a thin oblique impinging slot jet dryer at height. H_D, with a slot width of 50 μm ejecting nitrogen with a gas flow rate u_0 e). Schematic of the novel, alternative drying system, comb nozzle (CN) drying method is shown in d). The drying conditions are precisely defined via a 20×20 cm^2 nozzle array pattern consisting of hexagon-shaped jets (gas outlets, red) surrounded by slits for the local removal of the drying air (gas inlets, blue). This methodology allows to precise control of drying rates via a height. H_{CN}, a gas temperature T_{CN}, ejection of the GB inert atmosphere with an adjustable heat transfer coefficient α_{CN} f), the latter being a figure of merit for the solvent removal. The formation of the perovskite thin film during gas-assisted drying is optimized for both alternatives, resulting in visibly similar homogeneous, pinhole-free perovskite thin films shown in photographs g, h). Inhomogeneities due to accumulated solution by the gas backflow of the slot jet and edge effects are marked in Figure 1g (hatched in red and green, respectively). Microscopic morphological differences are discussed in section 2.3.

testing as well as already utilized in other experimental contexts by Kumberg et al.[47,48,50,51] The specific in-house CN dryer system of this work is inhabited in an in-house Glovebox system, meaning the drying circle is fully integrated in the inert atmosphere. During this work, the CN drying parameters are – iteratively with

perovskite precursor solution systems – optimized for controlled gas-assisted drying of perovskite absorber layers (Figure S3, Supporting Information). The drying nozzle height allows the extension of the optimal drying regime providing the mass transfer threshold for 2-step processes without leaving unwanted lateral

**ADVANCED
SCIENCE NEWS**

www.advancedsciencenews.com

**ADVANCED
ENERGY
MATERIALS**

www.advenergymat.de

patterns on the perovskite thin film layer (Figure S3 (Supporting Information) – height variation). Furthermore, herein, CN drying can be subdivided into two steps. First, a predrying driving step, while the substrate with the soaking wet film is driven with maintaining $\nu_{1,2}$ underneath the CN dryer. While driving underneath the CN hood, the CN dryer is switched on in the respective stationary drying conditions, leading to homogenous drying conditions (driving smoothens out the rest of the hexagonal pattern) while most of the IPA evaporates. Afterward, the rest of the solution is dried stationary for several minutes as a second step. The parameter optimization of both alternatives, slot jet, and CN drying, results in the formation of dark, specular reflecting perovskite thin films during gas-assisted drying and results in homogeneous, pinhole-free perovskite thin films with slightly visible alterations as depicted in Figure 1g,h. Inhomogeneities due to accumulated solution by the gas backflow of the slot jet and edge effects are marked in Figure 1g (hatched in red and green, respectively). After slot jet drying, even to the bare eye, a distinct transition of thin-film morphologies is visible. In the beginning and at the edges, the thin film appears diffusely reflective, occasionally yellow, then transitions into a dark, specular reflecting area, and finally a dark gray diffuse area is visible coming along with a higher thickness (Figure 1g). During CN drying, the delay of the drying and pushed-back liquid can be fully avoided, providing a distinct transition of thin-film morphologies to an extended dark, specular reflecting area. Dark gray diffuse edges are visible only at the far ends of the substrate (Figure 1h).

2.2. Optoelectronic Performance Heatmap

A precise optoelectronic comparison of the two drying approaches reveals significant distinctions, validating the different morphological qualities in section 2.1. Specifically, we investigate the coating of a substrate (100×100 mm^2) at a coating velocity of 6 mm s^{-1} for both steps of the triple cation precursor solution (for further details, see experimental section) and at a PCE-optimized drying velocity of 1.5 mm s^{-1}, a nozzle height of 0.3 cm, an angle of 15° and gas flow rate of 32 m s^{-1} during slot jet drying. We compare the results to a PCE-optimized CN drying with height $H_{CN} = 10$ mm, drying gas temperature $T_{CN} = 80$ °C, and heat transfer coefficient $\alpha_{CN} = 110$ W m^{-2} K^{-1} for 5 min. The height is optimized maintaining the maximum mass transfer without leaving comb-shaped patterns on the substrate. The temperature is regulated such that fast drying is provided. However, increasing the temperature further will increase the crystal growth rate, which has an adverse effect on obtaining nucleation-dominated morphologies. Reaching faster drying conditions, one alleviating strategy can be the usage of even lower boiling point solvents. Since these evaporate faster, nucleation gets more dominant toward crystal growth compared to high boiling solvents, even at lower mass transfer coefficients. The maximal heat transfer coefficient of ≈ 120 W m^{-2} K^{-1} experimentally required during drying perovskite precursors in this work, is still within the range of typical industrial-scale dryers[38] (more detailed information about the CN drying optimization can be found in, Figure S3, Supporting Information).

To validate the impact of different drying approaches on the performance of perovskite solar cells, we fabricate and analyze devices with all-scalable methods and an active area of 10.5 mm^2 (**Figure 2**) based on the architecture ITO/2PACz/Pero/C$_{60}$/BCP/Ag (experimental section). The devices are subsequently measured under a solar simulator and traced back to the original geometrical position of the substrate. PCE-heatmaps of the coated and alternatively dried substrates are presented in Figure 2a,b, showing the PCE distribution according to different morphology formations in setups depicted in Figure 1. Corresponding J_{sc}-, V_{oc}- and FF-heatmaps of CN- and slot jet-dried PSCs show similar relative variations concurring to respective morphologies (Figure S4, Supporting Information).

As mentioned above, after slot jet drying, a distinct transition of thin-film morphologies is visible. In the beginning and at edges, the thin film appears diffusely reflective, then transitions into a dark, specular reflecting area associated with high PCE-values, and finally a dark gray diffuse area is visible coming along with a higher thickness and lower PCE-values. This combination of the different drying states explained above on one substrate is determining for perovskite upscaling. We account their occurrence to the following difficulties that occur in batch-to-batch processing. Either i) the wet thin film shows small fluctuations and cannot be dried homogeneously without the prior fully evolved and 2-D aligned meniscus, ii) the drying condition is not set fast enough, since the controlled drying can only take place when the substrate is precisely underneath the slot or, iii) the wet thin film is pushed back by the inevitable gas backflow, disturbing the homogeneity of the dried thin film leading to unwanted patterns or thickness variations. The gas backflow is almost inevitable, e.g., due to disturbing but functional components in the nozzle, the inside contour having edges and certain radii of curvature inducing stalling and turbulences of the gas flow as well as the tendency of air flowing from high to low-pressure regions.[39,40] Therefore, most of the thin film is optimally dried directly under the nozzle center, whereas at the end of the drying process, the solution is accumulated and drying occurs a significant distance after the nozzle center has passed, drying basically without gas assistance. The ink at the edges of the substrate dries chaotically mainly because of drying rate variations on the edges of the slot nozzle causing a significant decrease in PCE (<13%). As a response, during precisely controlled CN drying, the delay of the drying pushed back liquid, and edge effects can be avoided, providing a distinct transition of thin-film morphologies to a significantly larger dark, specular reflecting area. Dark gray diffuse edges are only visible at the far ends of the substrate. The reason is the 2D drying system, 1) covering the entire substrate at once and 2) provides several precisely flow-controlled hexagonal jets without a problematic gas backflow, which would push liquid to the rear part of the substrate. This work shows that the CN drying elucidates the drying dynamics during the morphology formation, compared to a single high-pressure slot jet. The narrow operational window or almost peak of mass transfer being present at a critical thin-film thickness at the right time to which the drying parameters need to be fine-tuned, is now 2D widened. Still, the right timing of a certain threshold heat (and accordingly mass) transfer underneath the array of hexagonal jets, requires a precise tuning of the drying parameters.

Remarkably, we succeed in showing an extension of the optimally dried area in demonstrating a significant increase in the
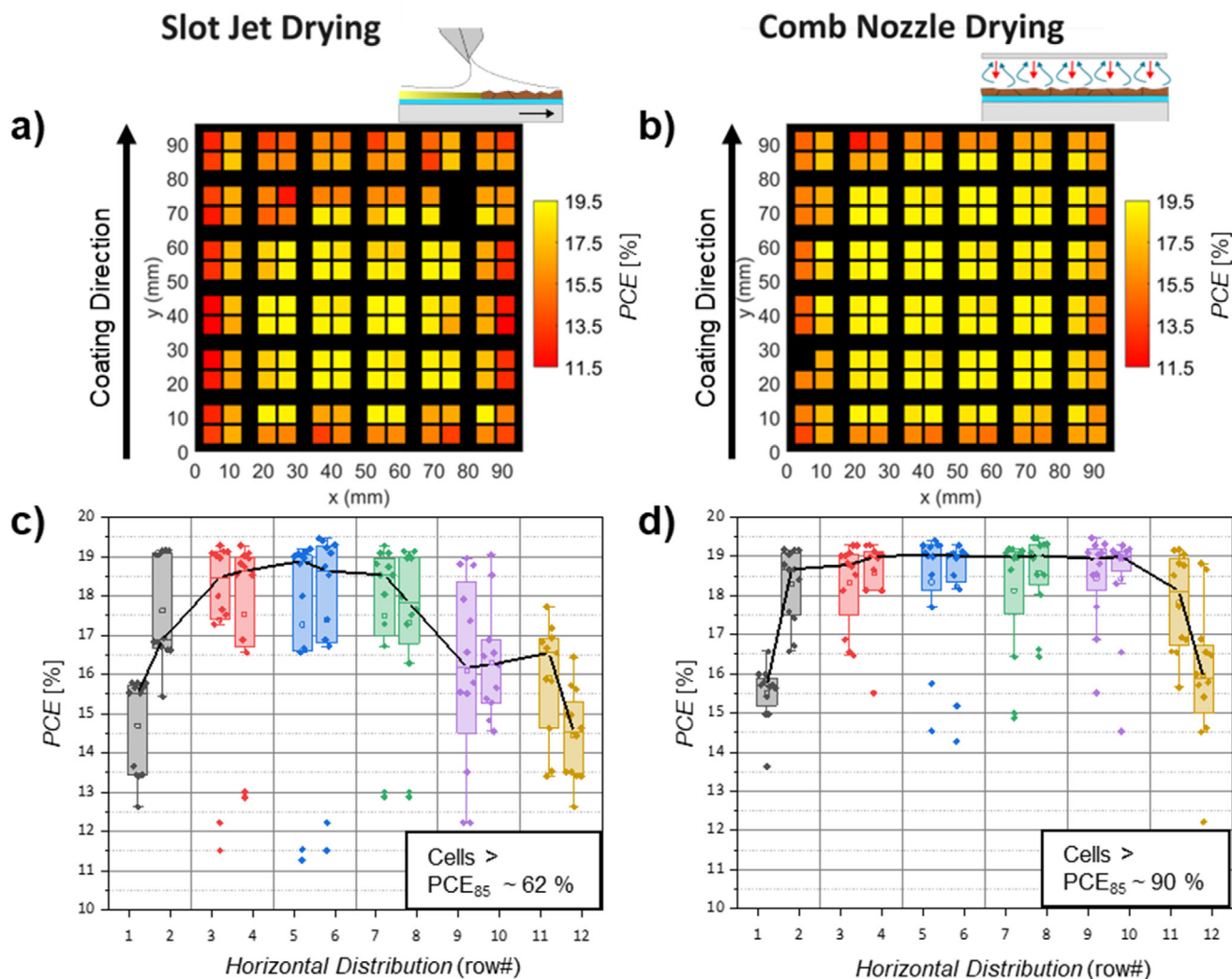
2500923 (5 of 15)

ADVANCED
SCIENCE NEWS

www.advancedsciencenews.com

ADVANCED
ENERGY
MATERIALS

www.advenergymat.de

Figure 2. PCE-heatmaps a, b) of solar cells (active area of 10.5 mm² (ITO/2PACz/Pero/C$_{60}$/BCP/Ag)) built from the respective perovskite absorber thin films (100 cm²), depicting the performance of devices traced back to the exact position on the substrate. The devices are fabricated with the setup shown in Figure 1 at the PCE-optimized drying gas flow velocity. $u_0 = 32$ m s^{-1}, dynamic drying speed of 1.5 mm s^{-1} and nozzle height 0.3 cm for slot jet drying. For CN drying, the PCE-optimized parameter set includes the height $H_{CN} = 10$ mm, drying gas temperature $T_{CN} = 80°$C, and heat transfer coefficient $\alpha_{CN} = 110$ W m^{-2} K^{-1}. PCE values vary strongly in the upper part and on the edges (red color code) after drying with a single slot jet according to morphological variations (a). Decreases in PCE can be significantly reduced, due to the control of drying rates via CN drying, as seen in PCE-heatmap (b). Significantly more of the perovskite thin film is optimally dried (yellow color code) directly under the nozzle centers and the solution is only accumulated on the far edges during the drying process. Corresponding J_{sc}-, V_{oc}- and FF-heatmaps of CN- and slot jet-dried PSCs are shown in, Figure S4 (Supporting Information). Cutting the heatmaps horizontally results in horizontal PCE-distributions c, d). PCEs of PSCs fabricated with slot jet-dried thin films are highest in the case of optimal drying in the middle of the samples (rows 3–8) and drop significantly in rows 1 & 2, and 9–12 (c). After CN drying, only rows 1 and 12 show a light PCE drop, increasing the PCE$_{85}$ yield significantly from 62% to 90% (d).

PCE$_{85}$-yield via CN drying compared to conventional slot jet drying (90% vs 62%, respectively), while champion solar cells of both drying methods remain reaching up to 19.6%. We measure significant PCE differences during the two drying methods at the exact positions where the corresponding morphology evolved, consistently with the dark, specular reflecting area being significantly larger and only far edges showing a dark gray diffuse area during CN drying. Illustratively, PCE-heatmaps (Figure 2a,b) show the significant minimization of PCE-loss during CN drying, due to the prevention of a backflow-induced higher thickness at the end of the coating (Figure 2a compared to Figure 2b at the top of the substrate) and fewer edge effects due to inconsistent drying rates of the slot jet. Slicing the substrates in horizontal rows from bottom (1) to top (12), the influence of the backflow during slot jet drying gets even more prominent (Figure 2c,d). After slot jet drying, there is a strong decrease in the mean PCE starting at row 9, dropping to ≈16% and showing a significantly higher PCE variance than row eight, implying the inhomogeneous drying pattern onward this row (Figure 2c). Whereas mean PCE-values ≥ 18% are only present in rows 3–8 for slot jet drying, the high-PCE region is significantly enhanced during CN drying, reaching from rows 2–11 (Figure 2d).
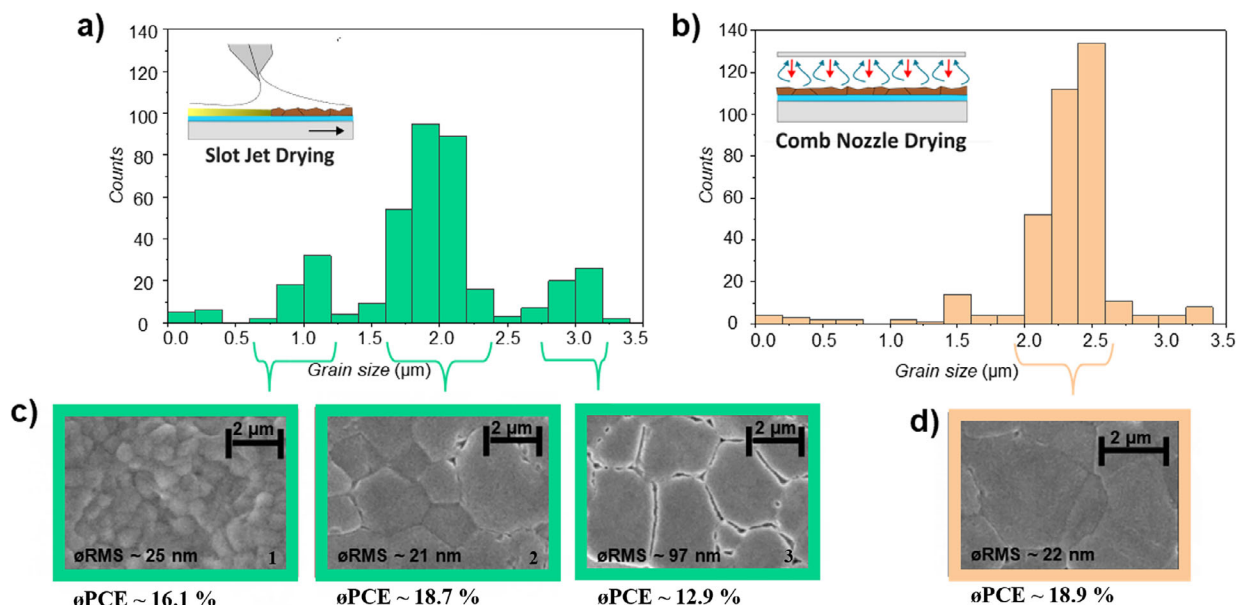
**ADVANCED
SCIENCE NEWS**

www.advancedsciencenews.com

**ADVANCED
ENERGY
MATERIALS**

www.advenergymat.de

Figure 3. Grain size distribution a, b) of the microscopic morphology via atomic force microscopy (AFM) and investigation via a scanning electron microscope (SEM) c, d) reveal the different drying characteristics, i.e., thin-film morphologies after slot jet (left, green) and comb nozzle (CN) drying (right, orange). After slot jet drying, three different drying regimes occur, resulting in a relatively wide grain size distribution (a). In comparison, the mean grain size distribution after CN drying is relatively narrow (b). Reproducible, slot jet-dried substrates contain i) homogeneous and dense thin film with grain sizes ≈2 µm (optimal area, øPCE = 18.7%), ii) areas with smaller grain sizes (øPCE = 16.1%), and iii) inhomogeneous layers with pinholes and high roughness (≈97 nm, øPCE = 12.9%) (c). Investigation of the morphology via SEM reveals that grain sizes are significantly larger and densely packed for morphologies corresponding to better PCE values compared to the two differently definable morphology regions. SEM of CN-dried morphologies reveals that grain sizes are mainly between 2 and 2.5 µm and densely packed throughout the major part of the substrate with a roughness of ≈22 nm (comparable to the optimal drying region after slot jet drying –≈21 nm, see also XRD-measurements in, Figure S12, Supporting Information) (d). Consistently, mean PCE values of solar cells fabricated on respective areas are similar (øPCE = 18.7% and 18.9%, respectively).

The generally higher PCE variances (difference of the box sizes of all respective rows in Figure 2c,d and higher decrease of PCE on the very edges of the substrates during slot jet drying (compare outliers of Figure 2c,d), validate the precise control of the drying rates and constructional advances by the CN technique, underlining the improved usability for full-area needing applications, such as flexibly shaped substrates or tandem devices. However, rows 1 and 12 in Figure 2d illustrate that there still is room for improvement at the far edges of CN-dried substrates. Addressing these edge effects, one way could be the installation, implementation, and optimization of systematic "wobbling" (systematically driving the substrate or CN hood back and forth during a specific time of drying), instead of a driving and stationary phase of drying. As a result, the hexagonal pattern of the drying system and the effects of the corners of the drying pattern itself could be smoothened out more systematically and individually to the material system. Especially on the edges, which– for uniformity— need to withstand more drying effects and the influence of particles from transporting the substrate, this could lead to more homogeneity over the whole substrate. Furthermore, additives resulting in more consistent distributions of the precursor solution onto the substrate or the optimization of nanoparticle application on tandem devices to control fluidics at the edges could further reduce edge effects. Since high-quality thin films usually result in improved stability (PCE-measurement in the MPP is shown in, Figure S11, Supporting Information), we stored champion devices in an inert atmosphere for further stability testing. In, Figure S16 (Supporting Information), we show a 10 h MPP track-

ing of a representative CN-dried device from the optimal drying area 172 days after fabrication, validating the high perovskite thin film quality with a PCE still reaching >90% of the initial PCE.

2.3. Correlation of Surface Morphology and Power Conversion Efficiency

As introduced in 2.1 and 2.2, variations of the perovskite absorber quality are apparent on substrates processed with different drying methods. To determine the impact of the respective morphologies on the performance of perovskite solar cells, we correlate the mean PCE of fabricated test cells with morphological characteristics.

As a result, we find that the variations of the PCE values (Figure 2) correlate to significant differences in microscopic morphology and grain size distributions (**Figure 3**). The mean grain size for CN dried films averaged over 100 cm² test devices increases up to ≈2.5 µm (Figure 3d) compared to the slot jet dried mean grain size (≈2 µm, (Figure 3c-2)), increasing the diffusion length of charge carriers and therefore, mean PCE-values. Consistently with the PCE trend after slot jet drying, microscopic investigations of the morphology via scanning electron microscope (SEM) reveal clearly that grain sizes and roughness are significantly increased (≈3 µm and ≈100 nm, respectively) compared to CN-dried thin films. Additionally, there are pinholes and inhomogeneities develop when the thin film is post-dried due to an increased thickness of the pushed liquid during slot jet drying

ADVANCED
SCIENCE NEWS
www.advancedsciencenews.com

ADVANCED
ENERGY
MATERIALS
www.advenergymat.de

(Figure 3c-3). Post-drying is well known in the literature to be inoperative for a controlled drying behavior.[25] The wet thin film dries in an uncontrolled manner without the facile and reproducible gas-assisted drying technique. This insight is consistent with Figure 3. Simultaneously, microscopic investigations reveal that grain sizes are reduced ≤ 1 µm on a significant part of the slot jet-dried perovskite thin film (Figure 3c-1), indicating that nucleation starts too early. The reason can be an inevitable gas backflow, causing inconsistent drying rates. The decrease of the overall grain size (Figure 3c-1, SEM surface images), results in a decrease in the diffusion length of charge carriers, coming along with a reduced efficiency of respective solar cells, in this specific case by almost 3%.

Accordingly, mean PCEs of solar cells fabricated on respective areas of the substrate confirm that the PCE has a similar optimum for both drying approaches (øPCE = 18.7%, Figure 3c-2 and 18.9%, Figure 3d for slot jet and CN drying, respectively). During CN drying, only ≈10% show grain sizes apart from this regime without forming any bulk of grain size formations below or above 2–2.5 µm or inhomogeneous thin film with pinholes. Therefore, the main part (≈90%) of CN dried substrates is comparable to the optimal drying region of slot jet-dried substrates (see also XRD-measurements in Figure S12, Supporting Information), showing a significantly lower amount of suboptimal drying regimes with either small grain size or inhomogeneities. This morphological change implies an extension of the optimal drying region due to CN drying.

Additionally, besides having more counts of the optimal grain size distribution during CN drying, the lack of bulks of inhomogeneous thin films (roughness ≈100 nm, øPCE = 12.9%) and morphologies with small grain sizes (< 1 µm, øPCE = 16.1%) is significant. Both result in reduced cell efficiencies and are prominent as separate drying regimes after slot jet drying. All slot jet-dried substrates prominently come with two suboptimal drying regimes of first, inhomogeneities and pinholes (øPCE = 12.9%, Figure 3c-3) and second, significantly smaller grain sizes (øPCE = 16.1%, Figure 3c-1), both resulting in reduced cell efficiency. Conclusively, CN drying obtains a relatively larger area of high-quality perovskite thin film (Figure 3), since PCE-decreasing regimes are significantly less prominent than after slot jet drying. These results demonstrate the importance of suppression of the gas backflow and control of drying rates, preventing suboptimal drying characteristics. In summary, CN dried perovskite thin films profit of the precise drying rate control and prevention of disturbing gas backflows. The array of flow-controlled hexagonal gas in and outlets reduces the effect of suboptimal drying regimes, significantly enhancing the optimal area of reproducible high-quality perovskite thin film. We demonstrate obtaining upscaled high performances of PSCs achieving an overall homogeneous drying behavior on areas of 100 cm².

2.4. Module Fabrication on Extended Optimal Drying Area

As discussed in sections 2.l–2.3, the specifics of drying for SD-coated substrates are crucial for the optimal perovskite thin film formation. Indeed, the morphology formation as well as the resulting performances of solar cells, built from incorporating parts of presented suFor the material system discussed in sectibstrates,

confirm that the optimal drying regime can be extended and controlled via a sophisticated drying system. With a parameter set (height, gas flow temperature, and heat transfer coefficient) for a given SD-coated material system, a homogenous perovskite thin film on upscaled areas can be provided via the 2-D CN drying system (section 2.2). For the material system discussed in section 2.1 and 2.2, evolving in perovskite absorber with a bandgap of 1.63 eV, a height $H_{CN} = 10$ mm, drying gas temperature $T_{CN} = 80$ °C and heat transfer coefficient $\alpha_{CN} = 110$ W m^{-2} K^{-1} provides the optimum in terms of morphology formation reflected in the champion PCE of 19.5% and 90% PCE$_{85}$ yield of PSCs fabricated on test areas of the respective substrates (Figure 2b).

Demonstrating the importance of adequate drying for scalable techniques during 2-step depositions, this parameter set is applied to four 50×50 mm² mini-modules which are embedded in a 100×100 mm² substrate, allowing a reflection of the performance on four quadrants. By depositing the perovskite thin film as described in section 2.1, we demonstrate the emergence of the extended optimal drying regime on all four quadrants (**Figure 4b**). A scheme of the solar module stack and its series of interconnections in the side view is shown in Figure 4a. The mini-modules have the conventional P1, P2, and P3 scribes by a nanosecond laser scribing, generating a geometrical fill factor (GFF) of 95% and consist of nine sub-solar cells with an aperture area of 144 mm² each (Figure 4a; Figure S7, Equation S1 (Supporting Information)). The identical stack with all-scalable methods as in section 2.1 and 2.2, only with thermally evaporated 75 nm gold back electrodes, is fabricated (experimental section, Figure S8, Supporting Information). A photograph of one exemplary test device after perovskite deposition on the perovskite side is shown in Figure 4d, illustrating the perovskite thin film after homogeneous drying with prompt crystallization. With the CN drying strategy, a PCE of up to 17.9% on an aperture area of 1296 mm² is obtained (Figure 4c). Significantly, perovskite mini-modules can be fabricated with all four quadrants reaching PCEs ≥ 17.6% and only a minimal deviation of maximal 0.3%$_{abs}$ (**Table 1**).

Compared to a simultaneously fabricated champion cell from a test area of the optimal drying regime (active area of 10.5 mm²), showing a PCE of 19.1% (Figure 4e), only ≈6% relative upscaling loss can be demonstrated, mainly explainable due to module scribing and interconnection resistances. Directly comparing both "active area PCEs" (meaning for the module: "aperture area PCE"/GFF = 17.9%/0.95 = 18.8% on an active area of 1231.2 mm² compared to 19.1% on 10.5 mm²) outlines the high perovskite thin film quality, achieving a loss in active area related PCEs of only 0.3%$_{abs}$ compared to small area PSCs. The characteristic values (J_{sc}, V_{oc}, FF) of the mini-module, including nine sub-solar cells, show minimal deviation compared to the reference cell, implying a high homogeneity during the coating and drying process (Figure 4c; Figure S6, Supporting Information). More specifically, each sub-solar cell of the mini-module has a V_{oc} of ~1.11 V, which is close to the V_{oc} obtained from the champion small-scale PSC (1.13 V). This small deviation indicates excellent homogeneity over the entire module area of the perovskite thin film and good interfaces of the stack with all scalable methods (Figure S8, Supporting Information). Extensive homogeneity on an exemplary representative module is also shown during photoluminescence-(PL-)measurements (Figure S13,
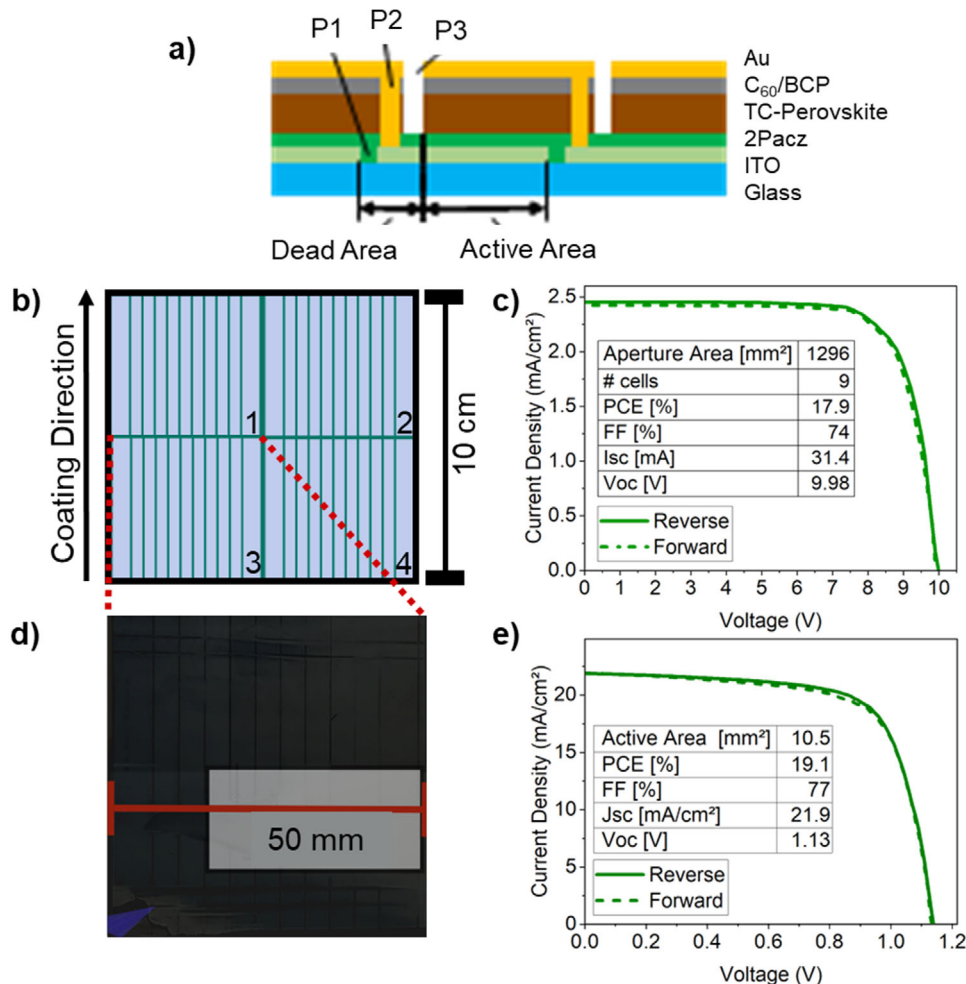
**ADVANCED
SCIENCE NEWS**

www.advancedsciencenews.com

**ADVANCED
ENERGY
MATERIALS**

www.advenergymat.de

Figure 4. Graphical illustration of an exemplary solar module stack (ITO/2PACz/Pero/C_{60}/BCP/Au) and its series interconnections in side view used in this work a). The mini-modules have the P1, P2, and P3 scribes by nanosecond laser scribing, generating a geometrical fill factor of 95% and consisting of nine sub-solar cells (aperture area 144 mm^2, respectively). A Schematic of the substrate with four laser-scribed mini-modules positioned at the quadrants of the ITO-covered glass on the movable table during coating and drying is shown in b). PCEs are consistent on the entire area which is reflected by a mean PCE of 17.7% $\pm$ 0.2%$_{abs}$ of perovskite modules fabricated on the quadrants of the respective substrates. The device performance (J-V curve) of an exemplary 50x50 mm^2 mini-module is shown in c). It shows only 6 % relative upscaling loss (17.9 % on 1296 mm^2 aperture area) compared to reference cells (19.1% with active area 10.5 mm^2). A photograph of one exemplary mini-module after perovskite deposition on the perovskite thin film side after homogeneous drying is shown in d). PCEs of perovskite modules 1, 2, and 4 are listed in Table 1 (1.63 eV). An exemplary reference solar cell fabricated on the same day, with identical coating and drying conditions as well as the same precursor solution and simultaneous device fabrication (19.1 %) is shown in e).

Table 1. Device performances of champion modules (1296 mm^2 aperture area) fabricated with the morphologies depicted in Figure 4d, providing the layer stack depicted in Figure 4a. The champion PCEs in the case of optimal drying of 1.63 eV triple cation (TC) perovskite absorbers reach 17.6%–17.9% resulting in a minimal deviation of performances over the entire substrate area. The scaling loss of the champion module toward a champion slot-die-coated reference cell built on the same day (19.1%) is 6.3%$_{rel}$, mainly due to module scribing and interconnection resistances. In the second row, the drying method is applied to precursor solutions providing a higher bandgap (1.68 eV). SD-coated PSCs reach up to 18% (18.5% spin-coated, Figure S6, Supporting Information). Employing CN drying to modules (1.68 eV) results in PCEs 16.5%–16.9% (1296 mm^2 aperture area) and shows only minimal deviations of performance over the entire substrate area. Remarkably, the relative scaling loss of the champion mini-module is 5.6%$_{rel}$ compared to a slot-die-coated champion reference cell built on the same day (17.9 %).

Bandgap [eV]	PCE$_1$ [%]	PCE$_2$ [%]	PCE$_3$ [%]	PCE$_4$ [%]	PCE Ref. cell [10.5 mm^2] [%]
1.63	17.7	17.7	17.9	17.6	19.1
1.68	16.9	16.6	16.8	16.5	17.9

**ADVANCED
SCIENCE NEWS**

www.advancedsciencenews.com

**ADVANCED
ENERGY
MATERIALS**

www.advenergymat.de

Supporting Information). Detailed information on the champion perovskite solar module is shown in Figure 4c and the efficiency deviation among the sub-solar cells themselves in the SI, Table S1, confirms homogeneity over the entire module area. The champion device's efficiency distribution of nine sub-solar cells shows that all sub-solar cells of the module have an efficiency higher than 17.7%, validating excellent drying conditions and homogeneity over the entire module area.

2.5. Toward Wide Bandgap Module Fabrication

For the application of perovskite absorbers in monolithic perovskite/silicon tandem configurations, optical simulations show that a wider bandgap ($E_g > 1.65$ eV) for optimal performance is required.[52–57] By changing the bromide/iodide ratio in a perovskite composition, the bandgap of the perovskite is tunable.[58,59] While in recent works, hybrid 2-step methods have been successfully developed to produce wide-bandgap PSCs for tandem applications, incorporating CsBr,[60–62] the incorporation of bromide in the solution-based 2-step method requires further effort to converge at high performances. In this regard, this work leverages knowledge from the process method of the perovskite top cells by Pappenberger et al., engineering wider bandgaps for the solution-based 2-step method on a laboratory scale.[63] The work is based on incorporating bromide in both deposition steps, the inorganic precursor deposition (step 1, $PbBr_2$) and the organic precursor deposition (step 2, FABr), increasing the bandgap of 2-step solution-processed perovskite thin films. Furthermore, the recipe is complemented with CsI in the bulk and LiF as surface passivation, enhancing the perovskite thin film crystallization, leading to improved charge carrier extraction and altogether resulting in a PCE exceeding 18.5% for $E_g = 1.68$ eV.[63] In this work, the effective, strategic recipe is slightly varied in terms of the exact distribution of given components for the first and second steps (experimental section). The need arises from an incremented activation energy needed for the migration of bromide anions in comparison to iodide anions during SDC.[41] Due to the arisen challenge of bromide diffusion into the lead halide layer during SDC compared to spin-coating, a higher amount of bromide and additional FAI, restraining the PbI_2 are added into the $PbI_2/PbBr_2$ solution. This componental variation in the first deposition step successfully optimizes the bromide incorporation and perovskite conversion for the scalable approach of SDC (experimental section, Figure S9, Supporting Information). Additionally, RbAc is introduced in step 1, thereby, metal cations reducing hysteresis and acetate anions significantly enlarging grain sizes, formatting $PbI_2/PbBr_2$ complex intermediate phases (experimental section).[41]

We succeeded in transferring the scalable deposition technique with the incorporated CN drying method to the 1.68 eV material system, slightly altering drying parameters to height $H_{CN} = 12$ mm, drying gas temperature $T_{CN} = 80$ °C and heat transfer coefficient $\alpha_{CN} = 100$ W m^{-2} K^{-1} (detailed heatmap with according parameters can be found in, Figure S17, Supporting Information), because of the slightly different material components and according to fluidic characteristics of the precursor solution. Regarding a similar PCE-heatmap as presented in Figure 2b, fabricating solar cells with active area 10.5 mm^2 on

100×100 mm^2 substrates reveals PCEs exceeding 18% (PCE-measurement in the MPP is shown in, Figure S11, Supporting Information) for $E_g = 1.68$ eV and demonstrates homogeneity over the entire substrate (Figure S5, Supporting Information).

The optimized CN drying parameter set is applied to four 50×50 mm^2 mini-modules which are embedded in a 100×100 mm^2 substrate as described for the 1.63 eV material system in section 2.4. Similarly, we demonstrate the extended optimal drying regime on all four quadrants and nine sub-solar cells on each module. Significantly, perovskite mini-modules can be fabricated with all four quadrants reaching PCEs up to 16.9% and only a minimal deviation of maximal 0.4% (Table 1, second row). Compared to a simultaneously fabricated champion solar cell from a test area (active area of 10.5 mm^2), showing a PCE of 17.9%, less than 6% relative upscaling loss can be demonstrated. The slight scaling loss is mainly explainable due to module scribing and interconnection resistances. Showing the minimal deviation compared to the reference cell implies a high homogeneity during the coating and drying process.

2.6. Implementation in 2T Tandem Devices

After successfully testing incorporated bromide anions into solution systems within the upscaled process of solar modules and thereby increasing the bandgap up to 1.68 eV in section 2.5, the developed strategy is implemented in the fabrication of planar monolithic perovskite/silicon tandem solar cells (TSCs). Due to the top-down penetration of the organic precursors in the second step, the 2-step method already facilitates the uniform coating of dense and pinhole-free perovskite thin films on silicon bottom solar cells, leading to higher achievable PCEs on a laboratory scale.[41,42] The employment in tandem devices represents one of the major challenges to push perovskite PV to an industrial level. Demonstrating the industrial applicability, we fabricate 16 silicon/perovskite tandem devices within one single SDC deposition step (as depicted in **Figure 5c**) via drying the 2-step processed perovskite thin film with the CN drying method on silicon planar bottom cells from Meyer Burger (Germany) AG (MB). With the CN drying method presented in 2.1–2.3, we demonstrate a systematic, universal, and adequate industrial process, applying it to drying processes of perovskite solution thin films on fragile substrates (< 0.1 mm).

The device architecture of the TSCs consists of the layer stack silicon bottom cell (MB)/ITO/MeO-4PACz/SiO_2-nanoparticles(-np)/Pero/LiF/C_{60}/BCP/SnO_2/IZO/Ag/MgF_2 (for details, see experimental section) with active areas of 1.04 cm^2 (with shadow mask during $J–V$ measurements: 1.0 cm^2). The complete schematic of the TSC layer stack is shown in Figure 5a. The $J–V$ characteristic of the champion device is depicted in Figure 5b, which exhibits good performance and high voltages. The champion tandem device reaches a PCE of 24.6% in the backward scan (24.4% in the forward scan) and provides a V_{OC} of 1.92 V, a J_{SC} of 18.1 mA cm^{-2} and a FF of 72%, demonstrating the high quality of the perovskite thin film (Figure 5b). Remarkably, we succeeded in depositing homogenous, high-quality perovskite thin films on all 16 tandems as depicted in the photograph (Figure 5e). The wettability is additionally improved via SiO_2-np on MeO-4PACz.[64] Performances are mainly limited by the low FF that requires
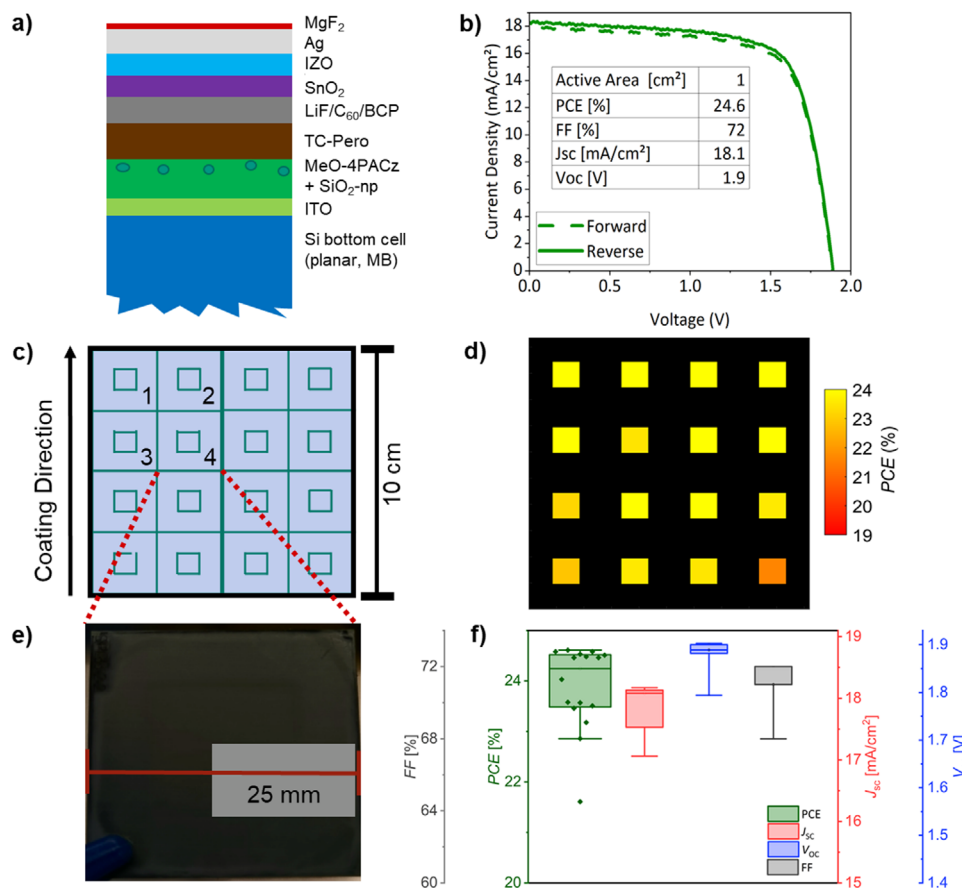
ADVANCED
SCIENCE NEWS

www.advancedsciencenews.com

ADVANCED
ENERGY
MATERIALS

www.advenergymat.de

Figure 5. Scheme of the TSC layer stack used in this work a). PCEs of the 25×25 mm^2 tandem devices reach up to 24.6 % (active area of 1 cm^2) demonstrating the high quality of the perovskite thin film as implied by J-V curve b). A 100 cm^2 substrate with 16 tandem devices schematically shows the positions of the silicon planar bottom cells + ITO and HTL on the movable table during perovskite thin film coating and drying (c). For the 1.68 eV precursor solutions, bromide is incorporated via PbBr2 and FABr in the first and second steps with CsI added in the inorganic precursor solution (7 mol.% CsI) and with slight componential variations (see section 2.5). LiF as surface passivation (1 nm) and an antireflective coating (90 nm MgF$_2$) are evaporated (for more details, see the experimental section). Optimal CN drying parameters are found to be: HCN = 12 mm, TCN = 80°C and αCN = 100 W m^{-2} K-1. The resulting PCE distribution on the exact positions of the champion substrate with 16 tandem devices is shown in the corresponding PCE-heatmap d). An exemplary photograph of one tandem device after perovskite deposition on the perovskite side is depicted in e). The photograph shows the tandem's perovskite thin film after homogeneous drying with sufficient crystallization. Statistical distributions of the median PCE (>24 %) and small PCE variances (0.7 %$_{abs}$) for all 16 devices imply that optimal, homogenous drying occurs on the entire substrate f). Equally, the FF, J_{SC}, and V_{OC} show median values of 71 %, 18.1 mA cm^{-2} and 1.89 V, respectively, with small variances (for details, see Table 2).

further investigation and optimization, whereas the V_{OC} is already in the expected range based on the results for the single-junction perovskite solar cells and the planar silicon cell. Additionally, the $J-V$ characteristic reveals a low hysteresis between backward and forward scans with a J_{SC} being close to current-matching. More specifically, the perovskite top cell has slightly lower J_{SC} than the J_{SC} of the silicon bottom cell ($\Delta J_{SC} = 0.2$ mA cm^{-2}, see EQE in, Figure S10, Supporting Information).

The qualitative distribution of all 16 device performances of the champion substrate (25×25 mm^2 tandem devices with an active area of 1.0 cm^2) is shown at the exact positions during SDC and drying on a PCE-heatmap (Figure 5d, corresponding to the schematic positions in Figure 5c). A detailed PCE bar chart of the tandem devices is shown in, Figure S15 (Supporting Information). All devices, except one outlier at the right corner, show a similar yellow color code, demonstrating the high

PCE provision of >23%. More specifically, the PCE median of >24% and small PCE variance of ≈0.7% $_{abs}$ for all 16 tandem devices underline that an optimal, homogenous drying regime is present on the entire substrate (Figure 5f and **Table 2**). Consistently, with prior observations on the CN dried PCE-heatmap of single junction devices (Figure 2b), no significant fluidic back-flow and only minimal edge effects are limiting the PCE, FF, J_{SC}, or V_{OC} (Figure 5d,f), implying that the perovskite crystallizes homogenously below the flow-controlled air nozzles on the entire substrate with optimized parameters. This enhancement of the high PCE yield indicates a straightforward implementation of the elaborated strategy on 2T TSCs. A prospective strategy for this methodology is to actively interfere with current drying parameters during processing through direct feedback loops. In this context, a concept of the correlation of the drying dynamics and yielded performance is a particularly interesting indicator to possibly automate and control the process immediately without

Table 2. Device performances of 16 tandem devices (1 cm^2 active area) of the champion substrate as well as median values and variances of PCE, FF, Jsc, and Voc of fabricated TSCs with the corresponding local distribution layer stack and morphologies depicted in Figure 5. The champion PCE reaches 24.6%. The median values and variances of the characteristic values calculated from the 16 representative tandem devices of the according morphology, underline the importance of controlled, homogenous drying conditions, showing especially high median PCE- as well as high median V_{OC}-values and low variances for all characteristic values.

$N_{Tandem} = 16$	PCE [%]	FF [%]	V_{oc} [V]	J_{sc} [mA cm^{-2}]
Median	24.0	71.0	1.89	18.1
Variance	0.7	0.8	0.02	0.3

wasting time and effort during the arduous production line, rapidly identifying a drift in the resulting morphology such that, for example, the gas flow temperature can be fine-tuned and thereby re-optimized immediately.

3. Conclusion

This work addresses the employment of spatially flow-controlled drying to large-area solution-processed perovskite thin films. It implements, demonstrates, and validates the applicability of a dedicated gas-assisted dryer system on homogenous 2-step processed SD-coated perovskite thin films, including the successful transfer to industrial-relevant perovskite PV, such as module and TSC fabrication. The specific CN drying method includes the GB-internal adjusted design of flow-controlled hexagon-shaped gas outlets surrounded by gas inlets. Thereby, gas inlets provide the local removal of the drying air according to the aero- and drying dynamics, precisely controlling drying rates. We identify and validate the parameter range of the proposed drying system with precisely defined drying conditions, needed for upscaling perovskite thin films. The main parameter set is defined by a dynamic height, gas flow temperature, and heat transfer coefficient, being fine-tuned for the given material system for an enlarged optimal drying regime.

Our study highlights the excellent drying conditions of the specifically shaped 2D array pattern by thorough local comparison of morphological and optoelectronic characteristics to a conventionally implemented oblique impinging slot jet drying system (sections 2.1–2.3). The latter is adjusted by a controlled height, angle, and overlapping lip configuration, reducing gas and corresponding fluidic backflow.[34] We identify a significantly more homogenous, dense drying behavior with grain sizes > 2 μm over the entire substrate area during CN drying. This improvement in drying characteristics is mainly attributed to 1) the enhanced flow control of the 2-D jet array and 2) an adjusted material/solvent system engineering for maximizing the benefits of the innovative drying system. Symbiotically, this leads to improved optoelectronic properties, pushing the single junction mean efficiency to > 19 % over an enlarged area compared to conventional slot jet drying. Consistently, by comparing the PCE$_{85}$-yields, we show that the optimally dried thin-film area increases from below 65 % (with slot jet drying) up to 90% (with CN drying), maintaining similar champion PCEs of ≈19.6%. Consequently, we demonstrate the resulting extended optimal drying regime, reaching up until the edges of the substrate, on four

50×50 mm^2 mini-modules in each quadrant of the sample (sections 2.4 and 2.5). Hereby, we validate the homogeneity and reproducibility by fabricating several substrates with laser-scribed mini-modules, providing a reproducible average PCE of ≈17.7% on a large area with only minimal area loss and prevented substrate waste, underlining the validity of the proposed methodology. Finally, we successfully show that the drying methodology is applicable to tandem-suited material systems (>1.65 eV) for monolithic perovskite/silicon TSCs (section 2.6). Remarkably, we demonstrate high TSCs efficiencies up to 24.6% with only a small PCE variance of ≈0.7%$_{abs}$ on an overall area of 100 cm^2. The results of this work validate the successful scaling via 2-step processes and flow-controlled drying for scalable, dynamic operation of perovskite fabrication lines. Overall, with both, integrated, fine-tuned dryers and material engineering, this work introduces a successful strategy for fabricating high-performance and homogenously upscaled p-i-n type wide-bandgap perovskite solar cells, modules, and planar perovskite/silicon TSCs, enhancing the facilitation for industrial solution-based production of high-quality perovskite (tandem) PV.

4. Experimental Section

Materials: 2PACz (TCI Chemicals (TCI), CAS: 20999-38-6), Lead iodide (PbI$_2$: TCI, CAS: 10101-63-0), Lead bromide (PbBr$_2$: TCI, CAS: 10031-22-8), Formamidinium iodide (FAI: Greatcell solar materials, CAS: 879643-71-7), Formamidinium bromide (FABr: Dyenamo, CAS: 146958-06-7), Methylammonium iodide (MAI: Dyenamo, CAS: 14965-49-2), Methylammoniumchloride (MACl: Dyenamo, CAS: 593-51-1), Cesium iodide (CsI: Alfa Aesar, CAS: 7647-17-8), urea (CH$_4$N$_2$O, SigmaAldrich), L-α-Phosphatidylcholin (α-LP: Sigma–Aldrich, CAS: 8002-43-5), Fullerene-C$_{60}$ (C$_{60}$: Sigma–Aldrich, CAS: 99685-96-8), Bathocuproine (BCP: Luminescence Technology (Lumtec), CAS: 4733-39-5), MeO-4PACz (TCI Chemicals (TCI), CAS: 2922526-56-3), Magnesium fluoride (MgF$_2$: Sigma–Aldrich, CAS: 7783-40-6), Lithium fluoride (LiF: ChemPur, CAS: 7789-24-4). All solvents including N,N-dimethylformamide, 99.8% (DMF, CAS: 68-12-2), Dimethyl sulfoxide anhydrous, ≥ 99.9% (DMSO, CAS: 67-68-5), 2-Propanol, 99.5%, (IPA, CAS: 67-63-0) were ordered from Sigma–Aldrich. Ethanol (EtOH) absolute anhydrous, ≥ 99.8% was ordered from VWR Chemicals.

Preparation of triple cation two-step perovskite solution and thin film (1.63 eV): The perovskite layer is deposited via a two-step slot-die coating. The inorganic solution of PbI$_2$:CsI (599.3 mg: 33.8 mg in 900 μL DMF and 100 μL DMSO) is completed by 5 vol% of α-LP solution (0.5 mg mL^{-1} pre-solved in DMSO)[49] and afterward SD-coated with according to parameters listed below. The SD-coated PbI$_2$:CsI thin films are subsequently annealed at 70 °C for 3 min in an inert atmosphere, resulting in a yellow-transparent layer.

After cooling down of the inorganic thin film, the formation of the perovskite is achieved by the cation solution on top of the lead iodide layer with SDC parameters below. On the day of deposition, the precursor solution of FAI:MABr:MACl (60:6:6 mg in 1 mL IPA) is completed by 3 mg mL^{-1} urea[34,65,66] and 5 vol% α-LP solution (0.5 mg mL^{-1} pre-solved in DMSO).[49] The respective drying approach is rapidly started after coating. After alternative drying approaches, as discussed in the result chapters, post-annealing outside of the glovebox under ambient conditions (at a relative humidity of 20%–50%) @ 150 °C for 15 min is provided.

The 2-step process (without additives) is based on the work of Li et al.[67]

Preparation of triple cation two-step perovskite solution (1.68 eV): The wide bandgap triple cation perovskites are prepared for the incorporation of bromide via PbBr$_2$ and FABr in the first and second steps, respectively. 1.245 M PbI$_2$ and 0.255 M PbBr$_2$ are dissolved in 930 μL DMF:DMSO (9:1 volume ratio). The inorganic solution is heated up to 130 °C for 30 min

**ADVANCED
SCIENCE NEWS**

www.advancedsciencenews.com

**ADVANCED
ENERGY
MATERIALS**

www.advenergymat.de

and vigorously agitated until all the powders are completely dissolved. After cooling down, 70 μL CsI solution (corresponds to 7 mol.% CsI, 390 mg mL^{-1} CsI in DMSO) is added to the inorganic solution. On the day of deposition, 5 mg/mL FAI, 1 mg mL^{-1} RbAc (RbAc and FAI added in the first step, forming a lead halide complex is based on the work of Chen, et al.[41]), and 5 vol% α-LP solution (0.5 mg mL^{-1} in DMSO)[49] as a surfactant are added to the solution. Altogether represents the basic perovskite solution. The basic perovskite solution is diluted in the ratio 2.5:1 in 4:1 DMF:DMSO for slot-die coating and is used in its concentrated form for spin coating references in order to guarantee similar thin film thicknesses. The basic solution is no older than one week. After the deposition, thin films are subsequently annealed on a hotplate at 70 °C for 1 min, resulting in a yellow-transparent layer.

The formation of the perovskite is achieved by SDC deposition of the cation solution on top of the inorganic layer with SDC parameters listed below. The organic cation solution is prepared by dissolving FAI (46.6 mg), FABr (25.3 mg), MAI (6.9 mg), and MACl (8.5 mg) in 1 mL IPA +. 4 mg/mL urea[34,65,66] and 5 vol% α -LP solution (0.5 mg mL^{-1} in DMSO)[49] as a surfactant which are added directly before SDC. The respective drying approach is started rapidly after coating. After alternative drying approaches, as discussed in the result chapters, post-annealing outside of the glovebox under ambient conditions (at a relative humidity of 20%–50%) for 15 min @ 150 °C is provided.

The incorporation of bromide via PbBr$_2$ and FABr in the first and second steps is based on the work of Pappenberger et al.[63] and slightly varied for SDC (Figure S9, Supporting Information).

SDC parameters of the 2-step process: The *1.63 eV* inorganic and organic precursor solutions are deposited subsequently by a 10 cm wide slot-die coater with an optimized slot-die width $b_{SD} = 0.1$ mm, slot-die gap $H_{SD} = 150$ μm and coverage-thickness as well as conversion-optimized dispense rates $d_{r1} = 0.6$ mL min^{-1} and $d_{r2} = 1.5$ mL min^{-1}, respectively (Figure S14, Supporting Information), over the substrate on a movable table with temperature ($T = 40$ °C) with optimized coating velocity $v_{1.1}$ and $v_{1.2} = 6$ mm s^{-1} (equal due to industrial applicability). If not stated otherwise, a 3 min thermal drying step of the inorganic solution at 70 °C is included before the SDC of the organic cation solution.

The *1.68 eV* inorganic and organic precursor solutions are deposited subsequently by a 10 cm wide slot-die coater with an optimized slot-die width $b_{SD} = 0.1$ mm, slot-die gap $H_{SD} = 150$ μm and coverage-thickness as well as conversion-optimized dispense rates $d_{r1} = 0.6$ mL min^{-1} and $d_{r2} = 1.8$ mL min^{-1}, respectively, over the substrate on a movable table with temperature ($T = 70$ °C) with optimized coating velocity $v_{1.1}$ and $v_{1.2} = 5$ mm s^{-1} (equal due to industrial applicability). If not stated otherwise, a 1 min thermal drying step of the inorganic solution at 70 °C is included before the SDC of the organic cation solution.

Processing of samples for coating experiments: 100×100 mm^2 ITO substrates (Luminescence Technology, sheet resistance 15 Ω sq^{-1}) are cleaned in an ultrasonic bath for 10 min in acetone and isopropanol, respectively. Subsequently, they are plasma etched for 3 min. Then, the samples are placed in the setup depicted in Figure 1. The coating is performed with a slot-die coater (from TSE Troller AG (TSE), Murgenthal, Switzerland) in length 100 mm, gap width 150 μm, and with parameters for the first and second steps given in section 2.1. Subsequently, the movable table is driven underneath either 1) a single slot jet (web speed is changed to the respective value and the N$_2$ flow is initiated with the chosen u$_0$ (section 2.1–2.3)) or 2) the movable table is driven underneath a comb nozzle dryer (CND from CN Drying Technology GmbH, Berlin, Germany) with adjustable height, temperature and heat transfer coefficient as described in section 2.1–2.5.

Fabrication of single-junction perovskite solar cells: The planar p-i-n type PSCs with the layer stack glass/ITO/2PACz/Pero/C$_{60}$/BCP/Ag are fabricated as follows. 128 × 128 mm^2 glass substrates with 120 nm thick indium tin oxide (ITO) coating (Luminescence Technology, sheet resistance 15 Ω sq^{-1}) are laser structured, cut into 100×100 mm^2 substrates, and then precut into a 6 × 6 grid of 16 × 16 mm^2 substrates. Afterward, they are cleaned in an ultrasonic bath for 10 min in with deionized (DI) water with glass cleaner, acetone, and isopropanol, respectively. This is followed by a 3 min oxygen plasma treatment before the deposition of the hole

transport (HTL) layer. Subsequently, the HTL (2PACz, 6 nm thickness) is thermally evaporated and deposited using a thermal evaporation system at a pressure of 5 × 10^{-7} mbar with a deposition rate of 0.05–0.2 A s^{-1}. Then, the perovskite coating experiments are conducted as explained in the respective sections. All perovskite absorber layers are deposited on the substrate with the solution-based two-step deposition method. After annealing, 1 nm LiF is thermally evaporated at an evaporation rate of 0.1–0.2 Å s^{-1} at a pressure of ≈10–6 mbar for the samples with LiF as surface passivation. The scalable device fabrication is completed by thermally evaporating and depositing the electron transport layer (ETL) – Fullerene (C$_{60}$, 25 nm thickness) and bathocuproine (BCP, 5 nm thickness) – using a thermal evaporation system at a pressure of 5 × 10^{-7} mbar with a deposition rate of 0.4 and 0.3 A s^{-1}, respectively. Afterward, the substrates are cut into 36 respective 16 × 16 mm^2 substrates and sorted by nucleation and growth-dominated regions if required or sorted by the primary indication marking the exact location on the substrate. Finally, the back electrode (100 nm Ag with 1 A s^{-1}) is thermally evaporated with a shadow mask in a thermal evaporator. The active area of the solar cells is defined to 10.5 mm^2, completing the PSCs with four pixels per substrate, if not stated otherwise.

Processing of Perovskite/Silicon Planar Tandem Solar Cells (TSCs): Before depositing the HTL layer, the silicon planar heterojunction bottom solar cells from Meyer Burger (Germany) AG (MB, 25 × 25 mm) are cleaned with acetone and IPA. For the HTL layer, a 6 nm MeO-4PACz layer is thermally evaporated on the silicon bottom cell with an ITO layer. MeO-4PACz is deposited using a thermal evaporation system at a pressure of 5 × 10^{-7} mbar with a deposition rate of 0.05–0.2 A s^{-1}. In order to increase the wettability, SiO$_2$-nanoparticles (more specifically nanospheres) are spin-coated on the MeO-4PACz layer based on the work of Turkay et al.[64] More detailed, NanoXact Silica nanospheres (aminated, 20 nm, 5.2 mg mL^{-1} in ethanol) are diluted with ethanol to obtain a 0.1 wt.% suspension. The SiO$_2$ nanospheres suspension is statically spin-coated at 2000 rpm for 20 s on the MeO-4PACz. Afterward, the substrates are dried on a hotplate at 100 °C for 10 min.[64] The perovskite absorber layer (1.68 eV) is fabricated as mentioned above and as described in section 2.6. After CN drying and annealing, 1 nm LiF is thermally evaporated as surface passivation. For the ETL layer, 25 nm of C$_{60}$ and 5 nm BCP are thermally evaporated. A 35 nm SnO$_2$ layer prepared by atomic layer deposition (ALD) is used as a buffer layer. Subsequently, 90 nm sputtered IZO from an IZO target using 190 W power with pure Ar and O$_2$ at 1 mTorr is used as a transparent electrode, and the active area of 1.04 cm^2 is defined by the thermally evaporated Ag electrode (300 nm). In order to reduce the reflection losses, 90 nm MgF$_2$ as an antireflection layer is evaporated on top of the Ag.

Microscopic Thin-Film Characterization: SEM analysis pictures are taken at IMT, Campus North, KIT via a scanning electron microscope (Zeiss LEO1530) with an in-lens detector and an aperture size of 20–30 μm. The applied acceleration voltages for surface analyses range between 5 and 10 kV.

Current Density−Voltage (J−V) Measurements: The J−V measurements are all performed under AM 1.5G conditions. Specifically, J−V characteristics of the PSCs are measured with a class AAA xenon-lamp solar simulator (Newport Oriel Sol3A) and with a scan rate set at 0.6 V s^{-1} using a source meter (Keithley 2400) with an AM1.5G spectra (100 mW cm^{-2}). The solar simulator irradiation intensity is calibrated using a certified silicon solar cell (Fraunhofer ISE) equipped with a KG5 bandpass filter. The stabilized PCE of the PSCs is determined by the power output at a voltage close to the maximum power point (MPP) under continuous illumination for 5 min. It is determined by measuring the photocurrent close to the MPP by using a perturb and observing algorithm under continuous AM 1.5G illumination, while the temperature of the devices is controlled at 25 °C by a Peltier element connected to a microcontroller during the measurements. A shadow mask is used in order to define the active area for the single-junction PSCs. More detailed information can be found in.[68] A shadow mask with an area of 1.0 cm^2 is used for the 2T TSCs.

To evaluate the data, a mismatch factor is determined from the EQE curve and the solar simulator spectrum, and the J−V curves are corrected accordingly. The EQE is measured using a PVE300 photovoltaic QE system

(Bentham EQE system). A chopping frequency in the range of 560–590 Hz with an integration time of 500 ms for single-junction PSCs (800 ms for 2T tandems) to acquire the spectra in a wavelength range from 300 to 850 nm and 300 to 1200 nm is used for single-junction PSCs and 2T tandems, respectively. An illumination spot (0.74 mm for single-junction, 1.5 mm for 2T tandems) is used to obtain the average over possible variations in the EQE spectra. For measuring the EQE, a shadow mask with an area of 1.0 cm² is utilized for the 2T TSCs. The solar simulator and EQE measurements are performed in an inert atmosphere in an N_2-filled glovebox.

Supporting Information

Supporting Information is available from the Wiley Online Library or from the author.

Conflict of Interest

The author of this manuscript declares a potential conflict of interest. Philipp Scharfer and Philip Cavadini hold shares in the company CN Drying Technology GmbH. Bahram Abdollahi Nejand is an employee of Meyer Burger, a company that commercializes solar modules

Data Availability Statement

The data that support the findings of this study are available from the corresponding author upon reasonable request.

[1] NREL, https://www.nrel.gov/pv/assets/pdfs/cell-pv-eff-emergingpv.pdf (accessed: November 2024).

[2] A. K. Verma, *J. Ravishankar Univ. (Part-B: Science)* **2023**, *35*, 68.

[3] Y. Zhao, C. Zhao, X. Chen, T. Luo, M. Ding, T. Ye, W. Zhang, H. Chang, *J. Mater. Sci.: Mater. Electron.* **2020**, *31*, 2167.

[4] Garside M., https://www.statista.com/topics/1959/silicon/. (accessed: November 2024).

[5] S. Mann, M. de Wild-Scholten, V. Fthenakis, W. van Sark, W. Sinke, *Prog. Photovoltaics: Res. Appl.* **2014**, *22*, 1180.

[6] P. Nayak, S. Mahesh, H. Snaith, D. Cahen, *Nat. Rev. Mater.* **2019**, *4*.

[7] NREL, https://www.nrel.gov/pv/cell-efficiency.html. (accessed: November 2024).

[8] M. Moffeq, N. Thabit, *ZANCO J. Pure Appl. Sci.* **2019**, *31*.

[9] D. Deb, K. Bhargava, *Degradation, Mitigation, and Forecasting Approaches in Thin Film Photovoltaics*, United Kingdom: Academic Press, **2022**, p. 151.

[10] V. C. M. Duarte, L. Andrade, *Energies* **2024**, *17*, 3896.

[11] S. Ternes, T. Börnhorst, J. A. Schwenzer, I. M. Hossain, T. Abzieher, W. Mehlmann, U. Lemmer, P. Scharfer, W. Schabel, B. S. Richards, U. W. Paetzold, *Adv. Energy Mater.* **2019**, *9*, 1901581.

[12] F. Yang, D. Jang, L. Dong, S. Qiu, A. Distler, N. Li, C. J. Brabec, H.-J. Egelhaaf, *Adv. Energy Mater.* **2021**, *11*, 2101973.

[13] D. B. Ritzer, T. Abzieher, A. Basibueyuek, T. Feeney, F. Laufer, S. Ternes, B. Richards, S. Bergfeld, U. W. Paetzold, *Progr. Photovolt. Res. Appl.* **2021**, *30*, 3489.

[14] J. T. Matondo, H. Hu, Y. Ding, M. Mateen, G. Cheng, J. Ding, *Adv. Mat. Technol.* **2024**, *9*, 2302082.

[15] C.-F. Lin, D. S. Hill Wong, T.-J. Liu, P.-Y. Wu, *Adv. Polym. Technol.* **2010**, *29*, 20173.

[16] H. Peng, H. Hu, J. Ding, G. Cheng, J. Ding, *J. Coat. Technol. Res.* **2024**, *21*, 1649.

[17] J. T. Matondo, H. Hu, Y. Ding, G. Cheng, J. Ding, *Nano Energy* **2024**, *9*, 2302082.

[18] A. Verma, D. Martineau, E. Hack, M. Makha, E. Turner, F. Nüesch, J. Heier, *J. Mater. Chem. C* **2020**, *8*, 6124.

[19] NREL, https://www.nrel.gov/pv/module-efficiency.html (accessed: November 2024).

[20] S. Valsalakumar, A. Roy, T. K. Mallick, J. Hinshelwood, S. Sundaram, *Energies* **2022**, *16*, 190.

[21] K. Schötz, C. Greve, A. Langen, H. Gorter, I. Doğan, Y. Galagan, A. J. J. M. Breemen, G. H. Gelinck, E. M. Herzig, F. Panzer, *Adv. Opt. Mater.* **2021**, *9*, 2101161.

[22] I. A. Howard, T. Abzieher, I. M. Hossain, H. Eggers, F. Schackmar, S. Ternes, B. S. Richards, U. Lemmer, U. W. Paetzold, *Adv. Mater.* **2019**, *31*, 201806702.

[23] X. Liang, X. Zhou, G. Chuang-Ye, H. Lin, S. Satapathi, Q. Zhu, H. Hu, *Org. Electron.* **2022**, *106*, 106546.

[24] Y. Yu, F. Zhang, T. Hou, X. Sun, H. Yu, M. Zhang, *Sol. RRL* **2021**, *5*, 202100386.

[25] A. Babayigit, J. D'Haen, H.-G. Boyen, B. Conings, *Joule* **2018**, *2*, 2542.

[26] J. T. Matondo, H. Hu, Y. Ding, M. Mateen, G. Cheng, J. Ding, *Adv. Mater. Technol.* **2024**, *9*, 2302082.

[27] S. Qiu, M. Majewski, L. Dong, D. Jang, V. M. Le Corre, J. G. Cerrillo, O. J. J. Ronsin, F. Yang, F. Guo, K. Zhang, L. Lüer, J. Harting, T. Du, C. J. Brabec, H.-J. Egelhaaf, *Adv. Energy Mater.* **2024**, *14*, 2303210.

[28] M. Azhar, Y. Yalcinkaya, D. T. Cuzzupè, Y. A. Temitmie, M. I. Haider, L. Schmidt-Mende, *Mater. Sustain.* **2025**, *1*.

[29] D.-A. Le, K. Kala, T.-S. Su, N. Perumbalathodi, T.-C. Wie, *Sol. RRL* **2024**, *8*, 2400553.

[30] Y. Jing, H. Xiao-Jing, L. Dong-Xue, S. Biao, W. Peng-Yang, X. Sheng-Zhi, Z. Ying, Z. Xiao Dan, *Acta Phys. Sin.* **2024**, *73*, 20240561.

[31] J. Chen, J. Liu, Y. Li, P. Xu, L. Xie, Y. Meng, H. Wu, X. Shang, S. Zhao, J. Pan, C. Xiao, M. Yang, Z. Ge, *Adv. Funct. Mater.* **2024**, *34*, 2314652.

[32] N. Taherimakhsousi, M. Fievez, B. P. MacLeod, E. P. Booker, E. Fayard, M. Matheron, M. Manceau, S. Cros, S. Berson, C. P. Berlinguette, *npj Comput. Mater.* **2021**, *7*, 6124.

[33] S. Tang, J. Bing, J. Zheng, J. Tang, Y. Li, M. Mayyas, Y. Cho, T. W. Jones, T. C.-J. Yang, L. Yuan, M. Tebyetekerwa, H. T. Nguyen, M. P. Nielsen, N. J. Ekins-Daukes, K. Kalantar-Zadeh, G. J. Wilson, D. R. McKenzie, S. Huang, A. W. Y. Ho-Baillie, *Cell Rep. Phys. Sci.* **2021**, *2*, 100511.

[34] K. Geistert, S. Ternes, D. B. Ritzer, U. W. Paetzold, *ACS Appl. Mater. Interfaces* **2023**, *15*, 52519.

[35] G. Cotella, J. Baker, D. Worsley, F. De Rossi, C. Pleydell-Pearce, M. Carnie, T. Watson, *Sol. Energy Mater. Sol. Cells* **2017**, *159*, 362.

[36] M. Fievez, P. J. Singh Rana, T. M. Koh, M. Manceau, J. H. Lew, N. F. Jamaludin, B. Ghosh, A. Bruno, S. Cros, S. Berson, S. G. Mhaisalkar, W. L. Leong, *Sol. Energy Mater. Sol. Cells* **2021**, *230*, 111189.

[37] S. Ternes, J. Mohacsi, N. Lüdke, H. M. Pham, M. Arslan, P. Scharfer, W. Schabel, B. S. Richards, U. W. Paetzold, *ACS Appl. Mater. Interfaces* **2022**, *14*, 11300.

[38] P. Cavadini, P. Scharfer, W. Schabel, Proceedings of the 15th Int. Heat Transfer Conf., IHTC, Kyoto, Japan (10-15 August 2014). Connecticut, USA: Begell House Inc.

[39] V. Satheesha, B. K. Muralidhara, N. Abhilash, C. K. Umesh, *Int. J. Engineer. Sci. Res. Technol.* **2018**, *7*, 2277.

[40] J. Wang, T. Klinkberg, M. Teschner, D. Weirich, T. Koll, *12th Int. Conf. on Zinc & Zinc Alloy Coated Steel Sheet Austria: Austrian Society for Metallurgy and Materials,* June, **2021**.

[41] B. Chen, P. Wang, R. Li, N. Ren, W. Han, Z. Zhu, J. Wang, S. Wang, B. Shi, J. Liu, P. Liu, Q. Huang, S. Xu, Y. Zhao, X. Zhang, *ACS Energy Lett.* **2022**, *7*, 2771.

[42] Q. Li, Y. Zhao, W. Zhou, Z. Han, R. Fu, F. Lin, D. Yu, Q. Zhao, *Adv. Energy Mater.* **2019**, *9*, 1902239.

[43] V. Cimrová, M. Guesmi, S. Eom, Y. Kang, D. Výprachtický, *Materials* **2023**, *16*, 1049.

[44] J. Zhang, T. Bu, J. Li, H. Li, Y. Mo, Z. Wu, Y. Liu, X. Zhang, C. yi Bing, F. Huang, *J. Mater. Chem. A* **2020**, *8*, 8447.

[45] J. Chang, E. Feng, H. Li, Y. Ding, C. Long, Y. Gao, Y. Yang, C. Yi, Z. Zheng, J. Yang, *Nano-Micro Lett.* **2023**, *15*, 164.

[46] J. Chang, E. Feng, X. Feng, H. Li, Y. Ding, C. Long, S. Lu, H. Zhu, W. Deng, J. Shi, Y. Yang, S. Xiao, Y. Yuan, J. Yang, *Nano Res.* **2024**, *17*, 8068.

[47] Europäische Patentschrift EP2761240B1, https://www.kit-technology.de/fileadmin/user_upload/EP2761240B1.pdf (accessed: January 2024).

[48] P. Cavadini, P. Scharfer, W. Schabel, *Int. Heat Transfer Conf.* **2014**, *15*, 5125.

[49] Y. Deng, X. Zheng, Y. Bai, Q. Wang, J. Zhao, J. Huang, *Nat. Energy* **2018**, *3*, 560.

[50] J. Kumberg, M. Baunach, J. C. Eser, A. Altvater, P. Scharfer, W. Schabel, *Energy Technol.* **2021**, *9*, 2000889.

[51] J. Kumberg, M. Baunach, J. C. Eser, A. Altvater, P. Scharfer, W. Schabel, *Energy Technol.* **2021**, *9*, 2100013.

[52] G. E. Eperon, M. T. Hörantner, H. J. Snaith, *Nat. Rev. Chem.* **2017**, *1*, 12.

[53] Z. Wang, Z. Song, Y. Yan, S. F. Liu, D. Yang, *Adv. Sci.* **2019**, *6*, 1801704.

[54] E. Aydin, T. G. Allen, M. D. Bastiani, L. Xu, J. Ávila, M. Salvador, E. V. Kerschaver, S. D. Wolf, *Nat. Energy* **2020**, *5*, 851.

[55] M. Jošt, E. Köhnen, A. B. Morales-Vilches, B. Lipovšek, K. Jäger, B. Macco, A. Al-Ashouri, J. Krč, L. Korte, B. Rech, R. Schlatmann, M. Topič, B. Stannowski, S. Albrecht, *Energy Environ. Sci.* **2018**, *11*, 3511.

[56] F. Gota, R. Schmager, A. Farag, U. W. Paetzold, *Opt. Express* **2022**, *30*, 14172.

[57] S. Mariotti, E. Köhnen, F. Scheler, K. Sveinbjörnsson, L. Zimmermann, M. Piot, F. Yang, B. Li, J. Warby, A. Musiienko, D. Menzel, F. Lang, S. Keßler, I. Levine, D. Mantione, A. Al-Ashouri, M. S. Härtel, K. Xu, A. Cruz, J. Kurpiers, P. Wagner, H. Köbler, J. Li, A. Magomedov, D. Mecerreyes, E. Unger, A. Abate, M. Stolterfoht, B. Stannowski, R. Schlatmann, et al., *Science* **2023**, *381*, 63.

[58] J. H. Noh, S. H. Im, J. H. Heo, T. N. Mandal, S. I. Seok, *Nano Lett.* **2013**, *13*, 1764.

[59] T. J. Jacobsson, J.-P. Correa-Baena, M. Pazoki, M. Saliba, K. Schenk, M. Grätzel, A. Hagfeldt, *Energy Environ. Sci.* **2016**, *9*, 1706.

[60] X. Luo, H. Luo, H. Li, R. Xia, X. Zheng, Z. Huang, Z. Liu, H. Gao, X. Zhang, S. Li, Z. Feng, Y. Chen, H. Tan, *Adv. Mater.* **2023**, *35*, 2207883.

[61] L. Mao, T. Yang, H. Zhang, J. Shi, Y. Hu, P. Zeng, F. Li, J. Gong, X. Fang, Y. Sun, X. Liu, J. Du, A. Han, L. Zhang, W. Liu, F. Meng, X. Cui, Z. Liu, M. Liu, *Adv. Mater.* **2022**, *34*, 2206193.

[62] X. Y. Chin, D. Turkay, J. A. Steele, S. Tabean, S. Eswara, M. Mensi, P. Fiala, C. M. Wolff, A. Paracchino, K. Artuk, D. Jacobs, Q. Guesnay, F. Sahli, G. Andreatta, M. Boccard, Q. Jeangros, C. Ballif, *Science* **2023**, *381*, 59.

[63] R. Pappenberger, A. Diercks, J. Petry, S. Moghadamzadeh, P. Fassl, U. W. Paetzold, *Adv. Funct. Mater.* **2024**, *34*, 2311424.

[64] D. Turkay, K. Artuk, X.-Y. Chin, D. A. Jacobs, S.-J. Moon, A. Walter, M. Mensi, G. Andreatta, N. Blondiaux, H. Lai, F. Fu, M. Boccard, Q. Jeangros, C. M. Wolff, C. Ballif, *Res. Square* **2023**, *8*, 1735.

[65] A. Farag, R. Schmager, P. Faßl, P. Noack, B. Wattenberg, T. Dippell, U. W. Paetzold, *ACS Appl. Energy Mater.* **2022**, *5*, 6700.

[66] A. Farag, T. Feeney, I. M. Hossain, F. Schackmar, P. Faßl, K. Küster, R. Bäuerle, M. A. Ruiz Preciado, M. Hentschel, D. Ritzer, A. Diercks, L. Yang, B. Abdollahi, F. Laufer, R. Singh, U. Starke, U. W. Paetzold, *Adv. Energy Mater.* **2023**, *13*, 2203982.

[67] H. Li, C. Zuo, D. Angmo, H. Weerasinghe, M. Gao, J. Yang, *Nano-Micro Lett.* **2022**, *14*, 79.

[68] S. Gharibzadeh, I. M. Hossain, P. Fassl, B. A. Nejand, T. Abzieher, M. Schultes, E. Ahlswede, P. Jackson, M. Powalla, S. Schäfer, M. Rienäcker, T. Wietler, R. Peibst, U. Lemmer, B. S. Richards, U. W. Paetzold, *Adv. Funct. Mater.* **2020**, *30*, 1909919.

[69] N. Rolston, A. Sleugh, J. P. Chen, O. Zhao, T. W. Colburn, A. C. Flick, R. H. Dauskardt, *Front. Energy Res.* **2021**, *9*, 264.

[70] J. Li, J. Dagar, O. Shargaieva, M. A. Flatken, H. Köbler, M. Fenske, C. Schultz, B. Stegemann, J. Just, D. M. Többens, A. Abate, R. Munir, E. Unger, *Adv. Energy Mater.* **2021**, *11*, 2003460.

[71] P. J. Singh Rana, B. Febriansyah, T. M. Koh, B. T. Muhammad, T. Salim, T. J. N. Hooper, A. Kanwat, B. Ghosh, P. Kajal, J. H. Lew, Y. C. Aw, N. Yantara, A. Bruno, S. A. Pullarkat, J. W. Ager, W. L. Leong, S. G. Mhaisalkar, N. Mathews, *Adv. Funct. Mater.* **2022**, *32*, 202113026.

[72] J. Park, J. Cho, *Angew. Chem.* **2020**, *132*, 15427.